



Article

Distributed-Drive Vehicle Lateral-Stability Coordinated Control Based on Phase-Plane Stability Region

Jun Liu and Ang Dai *

School of Automotive and Traffic Engineering, Jiangsu University, 301 Xuefu Road, Zhenjiang 212013, China; liujun@ujs.edu.cn

* Correspondence: 2212104092@stmail.ujs.edu.cn

Abstract: The lateral stability control of vehicles is one of the most crucial aspects of vehicle safety. This article introduces a coordinated-control strategy designed to enhance the handling stability of distributed-drive electric vehicles. The upper controller uses active front steering and direct yaw moment-control controllers designed based on sliding-mode control theory. The lower controller optimally allocates control inputs to the upper controller, considering factors such as load transfer and tire load rate. It divides the stability region by relying on the phase plane and develops a coordinated-control strategy based on the degree of deviation of the vehicle state from the stability region. The results of the simulation experiments demonstrate that the proposed control strategy effectively improves handling stability under extreme working conditions.

Keywords: sliding-mode control; phase-plane stability region; yaw moment distribution

1. Introduction

The term “vehicle handling stability” refers to the ability of a vehicle to maintain good maneuverability and stability under driver operation. This encompasses the vehicle’s stability performance when turning, making sudden turns, or encountering adverse road conditions. The comfort and stability of a vehicle depend on the interaction between the driver and the environment. However, due to the non-linear characteristics of the vehicle and uncertainties in the driver’s interaction with the environment, stability can be lost in certain conditions. Therefore, electronic stability programs have been developed to address this issue in many vehicles. Electric vehicles with distributed drive have become the ideal platform for implementing electronic stability control systems due to their independent control of all four wheels, fast response times, and excellent controllability.

Active front steering (AFS) and direct yaw moment control (DYC) are often used to improve a vehicle’s lateral stability, and both control methods can be used independently for stability control. Active front-wheel steering (AFS) improves the vehicle’s ability to stabilize the ride by providing an additional front-wheel steering angle. Wu Tong [1] proposed an AFS control strategy based on vehicle-state estimation and mass identification to address the difficulty in measuring vehicle state and actual mass. Simulation results verified the effectiveness of the control strategy in dealing with changes in vehicle mass. A novel active forward-steering (AFS) control strategy was proposed by Zhang J [2] with the goal of improving the stability and maneuverability of a vehicles. This control strategy consists of two components: an upper controller and a lower controller. The upper controller uses Adaptive Recursive Integral Terminal Sliding Modal (ARITSM) control, which is highly robust and converges quickly.

DYC (directional yaw control) maintains vehicle stability by generating additional yaw moments through the difference in longitudinal forces between the two sides of the vehicle [3]. There have also been several studies on the effect of DYC on the stability performance of the vehicle chassis. The authors of [4] estimated the actual side inclination



Citation: Liu, J.; Dai, A. Distributed-Drive Vehicle Lateral-Stability Coordinated Control Based on Phase-Plane Stability Region. *World Electr. Veh. J.* **2024**, *15*, 202. <https://doi.org/10.3390/wevj15050202>

Academic Editor: Peter Van den Bossche

Received: 5 April 2024

Revised: 24 April 2024

Accepted: 4 May 2024

Published: 7 May 2024



Copyright: © 2024 by the authors. Licensee MDPI, Basel, Switzerland. This article is an open access article distributed under the terms and conditions of the Creative Commons Attribution (CC BY) license (<https://creativecommons.org/licenses/by/4.0/>).

angle using a non-linear disturbance observer and further designed a second-order sliding-mode (SOSM) controller, which positively experimentally verified that the proposed SOSM controller is more effective.

In paper [5], the author designed a center-of-gravity lateral-inclination angle based on Kalman filtering, estimated the wheel slip characteristics using Forgotten Factor Recursive Least Squares (FFRLS), and proposed a yaw torque control method with fuzzy rules to maintain the stability and comfort of the vehicle.

However, both control methods have their own drawbacks and limitations. For example, under conditions of high sideways acceleration, the effectiveness of AFS is compromised as the tires operate in the non-linear region, hindering its ability to improve stability. Similarly, during DYC intervention in the driving process, changes in longitudinal forces can impact vehicle speed, which can cause driver discomfort [6]. To achieve effective coordinated control, it is important to address the limitations of a single control system and reduce coupling while leveraging the strengths of each subsystem.

Numerous academic studies have investigated the control of AFS and DYC for four-wheel independent-drive trams. The focus has primarily been on integrated control [7–9] and coordinated control [10–12]. Zhang, L [13] developed a fast terminal sliding-mode AFS controller using the inverse stepping control method. This was then integrated with DYC to form an upper controller, with the lower controller outputting appropriate torque to each wheel. In one paper [14], the authors propose a control strategy for optimal allocation. The simulation results compare and evaluate the average allocation, dynamic allocation, and the optimization methods presented in the paper. The results indicate that the optimized method is more adaptable to changes in road conditions and vehicle dynamics and improves path-tracking accuracy.

In addition, fuzzy control is often used in the development of stability controllers [14]. For instance, Li [15] proposed a T-S fuzzy model to estimate unmeasurable state variables and designed a stability controller to enhance the system's robustness to parameter perturbations. The simulation results demonstrate that the designed controller is robust to parameter agitation. Moreover, [16] discusses lateral stability control while maintaining a slip rate within a reasonable range and considering various constraints. The study introduces a limit on the road attachment coefficient and limits the output torque of the motor. Some studies have also explored incorporating energy optimization into stability controller design [17]. This allows vehicles to maintain stability while also considering performance metrics such as motor energy consumption.

This paper focuses on distributed electric vehicles and presents a coordinated-control strategy based on sliding-mode control. Straight swing torque and an active front-wheel steering controller are designed, taking into account the constraints of ground attachment conditions and the maximum torque of the motor. Two controllers are developed for the operating range and coordination rules, using the critical angle as a boundary condition. Simulation experiments show that the coordinated-control strategy outperforms the ordinary integrated-control performance, fully utilizing the advantages of the control system and improving the stability of the vehicle's handling performance.

The main contributions of this paper include:

- (1) AFS and DYC stability controllers were designed using sliding-mode control to enhance the approach rate.
- (2) The deviation from the stability region is measured using a distance function based on the phase plane, and coordinated-control rules are formulated accordingly.
- (3) The output of the controllers is optimally allocated, considering vertical load transfer and tire loading during working conditions.

2. Vehicle-Dynamics Model

2.1. Seven-Degree-of-Freedom Vehicle-Dynamics Model

The handling stability of a vehicle is mainly affected by the transverse pendulum motion and the lateral motion. Therefore, a whole-vehicle-dynamics model, including

longitudinal, transverse, lateral, and four-wheel rotations, was established, as shown in Figure 1.

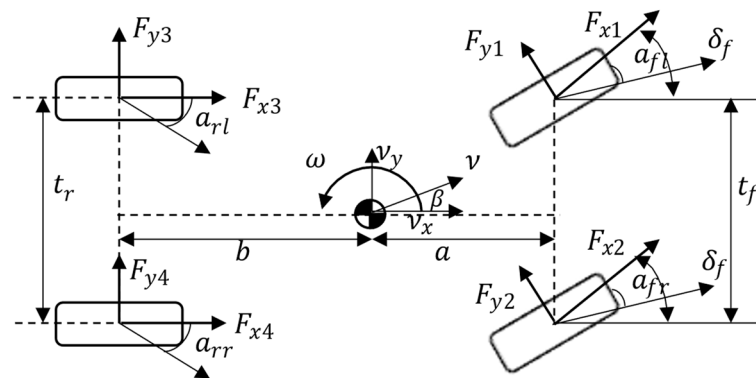


Figure 1. Seven-degree-of-freedom vehicle-dynamics model.

Longitudinal dynamic equation:

$$m(\dot{v}_x - v_y\omega) = (F_{x1} + F_{x2}) \cos \delta_f - (F_{y1} + F_{y2}) \sin \delta_f + F_{x3} + F_{x4} \quad (1)$$

Lateral dynamic equation:

$$mv_x(\dot{\beta} + \omega) = (F_{x1} + F_{x2}) \sin \delta_f + (F_{y1} + F_{y2}) \cos \delta_f + F_{y3} + F_{y4} \quad (2)$$

Yaw dynamic equation:

$$I_z\dot{\omega} = l_f(F_{x1} + F_{x2}) \sin \delta_f + l_f(F_{y1} + F_{y2}) \cos \delta_f + t_r(F_{x2} - F_{x1}) \cos \delta_f + \frac{1}{2}t_r(F_{y1} - F_{y2}) \sin \delta_f - l_r(F_{y3} + F_{y4}) \cos \delta_f + \frac{1}{2}t_r(F_{x4} - F_{x3}) \quad (3)$$

The rotational motion is shown in Figure 2. Its rotation equation is

$$J_\omega\dot{\omega}_i = T_{di} - F_{xi}R_i \quad (4)$$

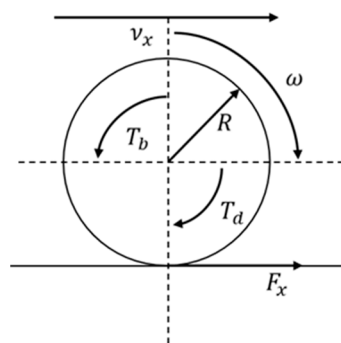


Figure 2. The vertical load on the tire.

m is the mass of the whole vehicle. R_i is the effective radius of the wheel, J_ω is the moment of inertia of the wheel, ω_i is the angular velocity of rotation, and T_{di} is the individual-wheel drive torque.

Vertical load on each wheel:

$$\begin{aligned} F_{z1}, F_{z2} &= m \left(\frac{gb}{L} - \frac{a_x h_g}{L} \right) \cdot \left(\frac{1}{2} \mp \frac{a_y h_g}{l_f g} \right) \\ F_{z3}, F_{z4} &= m \left(\frac{ga}{L} + \frac{a_x h_g}{L} \right) \cdot \left(\frac{1}{2} \mp \frac{a_y h_g}{l_r g} \right) \end{aligned} \quad (5)$$

2.2. Tire Model

The stability of a vehicle is greatly influenced by the non-linear characteristics of its tires. Therefore, accurately describing the side bias characteristics of the tires is crucial in determining the control effect of the stability controller. In this paper, we have adopted the Magic Tire formula [18,19] to describe the tire force due to its higher fitting accuracy and fewer parameters. The general expression form of the formula is as follows:

$$\begin{cases} F_y = D \sin(\text{Carctan}(BX - E(BX - \arctan(BX)))) + S_v \\ X = \alpha + S_h \end{cases} \quad (6)$$

in the above equation, F_y is the lateral force, D is the peak factor, C is the shape factor, B is the stiffness factor, E is the curvature factor, α is the sideslip angle, S_h is the horizontal drift, and S_v is the vertical drift factor. The specific expressions of these polynomials can be referred to in [20].

2.3. Drive Motor Model

The motor mounted on the wheels provides power for distributed vehicles and determines the vehicle's control effect [21,22]. This paper focuses on vehicle-dynamics modeling and simulation; therefore, the motor model's accuracy only needs to meet the driving brake-force output requirements during the simulation process. The motor's response characteristics are used to simplify it into a second-order response system. The Simulink model is shown in Figure 3, and the transfer function of the motor can be expressed as:

$$G(s) = \frac{T_d}{T_d^*} = \frac{1}{2\zeta^2 s^2 + 2\zeta s + 1} \quad (7)$$

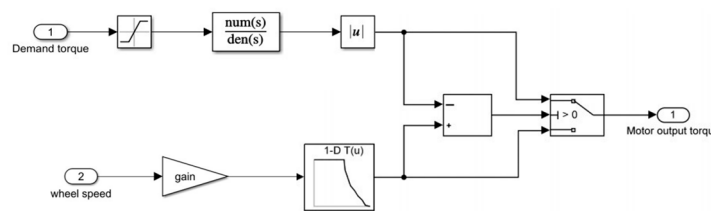


Figure 3. Motor speed and torque modeling.

T_d represents the actual torque, T_d^* represents the target torque, and ζ is the damping ratio for second-order systems and depends mainly on the motor's own parameters.

2.4. Reference Models

The linear two-degree-of-freedom model is simple to express but can describe the vehicle motion characteristics accurately under regular working conditions. It is commonly used as a reference model for the stability control of vehicle dynamics. Figure 4 illustrates the motion analysis of the model.

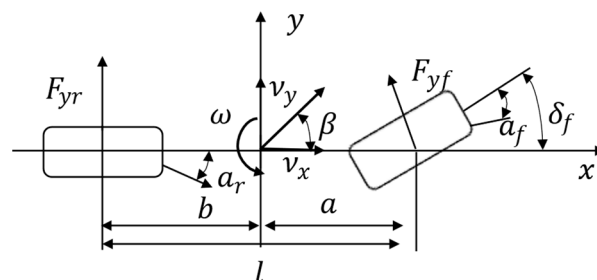


Figure 4. Two-degree-of-freedom vehicle model.

The continuous-time dynamic state-space system model can be derived by using the front-wheel angle as a system input:

$$\begin{pmatrix} \dot{\beta} \\ \dot{\omega} \end{pmatrix} = \begin{bmatrix} \frac{2k_f + 2k_r}{mv_x} & \frac{2ak_f - 2bk_r}{mv_x^2} - 1 \\ \frac{2ak_f - 2bk_r}{I_z} & \frac{2a^2k_f + 2b^2k_r}{I_z v_x} \end{bmatrix} \begin{pmatrix} \beta \\ \omega \end{pmatrix} + \begin{bmatrix} \frac{-2k_f}{-2ak_f} \\ \frac{mv_x}{I_z} \end{bmatrix} \delta_f \quad (8)$$

Using the uniform circular motion of the vehicle as the characteristic feature of steady-state steering, the yaw rate ω remains constant, and $\dot{v}_y = 0, \dot{\omega} = 0$. The ideal yaw rate can be deduced by the two-degree-of-freedom vehicle-dynamics model, taking into account the road-adhesion conditions and the actual condition of the tire under the ultimate working condition, using the substituted value from Formula (8):

$$\omega_d = \min \left\{ \left| \frac{v_x \delta}{l(1 + Kv_x^2)} \right|, \left| 0.85 \frac{\mu g}{v_x} \right| \right\} \cdot \text{sgn}(\omega) \quad (9)$$

$K = \frac{m}{l^2} \left(\frac{a}{k_r} - \frac{b}{k_f} \right)$ is the stability factor, sgn is the sign function, and μ is the road surface-adhesion coefficient.

The vehicle's ability to follow its intended path is significantly influenced by the presence of a sideslip angle. Additionally, an excessively large sideslip angle can lead to lateral instability. Therefore, researchers in numerous studies have designed the ideal sideslip angle to be 0 to optimize vehicle handling stability [23,24].

$$\beta_d = 0 \quad (10)$$

3. Controller Design

3.1. Longitudinal Speed Tracking

The aim of this paper is to focus on stability control, rather than conducting an in-depth study on speed following control. To achieve this, we adopted a PID controller design due to its simple structure and the ease of parameter adjustment. The speed tracking controller takes the driver's desired speed and current speed as inputs, and it outputs the generalized driving torque, with its control law as:

$$e_v = v_{\text{target}} - v_r \quad (11)$$

$$F_x = k_p e_v + k_i \int e_v dt + k_d d \frac{e_v}{dt} \quad (12)$$

In this paper, the values of k_p, k_i, k_d are taken as 500, 500, 10.

3.2. AFS Controller Design

AFS mainly functions in the stage where the non-linear characteristics of the tires are less pronounced, typically the side-slip angle of the vehicle's center of mass is small during this phase. Selection of traverse angular velocity deviation as a control target:

$$e_\omega = \omega - \omega_d \quad (13)$$

Selection of the integral sliding-mode surface:

$$s_\omega = e_\omega + \lambda_1 \int_0^t e_\omega dt \quad (14)$$

When choosing the convergence rate, we opt for a new form of enhanced convergence rate to reduce the jitter vibration phenomenon caused by the sliding-mode control near the sliding-mode surface.

$$\dot{s} = -\gamma_1 |s|^n \operatorname{sgn}(s) - \gamma_2 |s|^n \operatorname{sgn}(s) - \gamma_3 s \quad (15)$$

The final form of the additional front-wheel angle is obtained by combining Equation (8) and by calculation:

$$\delta_f = \frac{ak_f - bk_r}{I_z} \beta + \frac{a^2 k_f + b^2 k_r}{I_z v_x} \omega - \frac{ak_f}{I_z} \delta_f - \dot{\omega}_d + \lambda_1 (\omega - \omega_d) + \gamma_1 |s|^n \operatorname{sgn}(s) + \gamma_2 |s|^n \operatorname{sgn}(s) + \gamma_3 s \quad (16)$$

To further optimize the controller and jitter, the saturation function can be defined as:

$$\operatorname{sat}(s) = \begin{cases} 1, s > \Delta \\ ks, |s| < \Delta, k = \frac{1}{\Delta} \\ -1, s < -\Delta \end{cases} \quad (17)$$

During maneuvers such as turning, the vehicle experiences a change in the vertical load on the left and right tires. However, conventional active front-steering (AFS) systems often adopt an idealized approach when allocating additional front-wheel steering angles, treating the left and right supplementary front-wheel angles as equal. This approach may cause lateral force saturation on the inside wheel, while the potential of the outside wheel's lateral force remains underutilized. Consequently, this diminishes the vehicle's capability for extreme turning. To address this, a redistribution of the added steering angles for active front-wheel steering is proposed. This involves adjusting the steering angles by either reducing the angle on the inside wheel or increasing it on the outside wheel, enabling the outside wheel to contribute significantly to the required lateral force during turning:

$$\begin{cases} \delta_1 = \frac{\delta_f}{2} + \left(\frac{F_{z1} - F_{z2}}{F_{z1} + F_{z2}} \right) \frac{\delta_f}{2} \\ \delta_2 = \delta_f - \delta_1 \end{cases} \quad (18)$$

3.3. DYC Controller Design

As the tire side-deflection angle increases, it gradually exhibits non-linear characteristics. At this point, the lateral force provided by active steering approaches saturation, and the stability control effect cannot be achieved solely through AFS. Therefore, the direct yaw moment controller must intervene, considering both the error in the transverse pendulum angular velocity and the error in the lateral deflection of the center of mass. This combined error is defined as:

$$e = e_\omega + \tau e_\beta = (\omega - \omega_d) + \tau(\beta - \beta_d) \quad (19)$$

τ is not weight coefficients but is used to unify dimensions. In some studies, the above expression is used as the synthetic error to design the controller. However, this definition does not guarantee in all cases that e_ω and e_β are able to converge simultaneously. When $e_\omega = -\tau e_\beta$, the combined error e is in a state of convergence, but yaw velocity deviation and centroid side deviation exist simultaneously. To achieve the effect of convergence at the same time, we refer to the comprehensive error definition form and controller design method proposed by Chunyun F [25]:

$$e = s_1 = \frac{\varepsilon}{|\Delta\omega|_{\max}} |e_\omega| + \frac{1 - \varepsilon}{|\Delta\beta|_{\max}} |e_\beta| \quad (20)$$

In the above formula, ε is the weight coefficient. The maximum yaw velocity error $\Delta\omega_{\max}$ and side yaw angle error $\Delta\beta_{\max}$ allow for the stable running of the vehicle; they are

selected to unify the dimension. Meanwhile, their regularization is carried out to avoid a situation on which the comprehensive error is zero while the respective error is not zero.

$$\begin{aligned} \Delta M_z = I_z \left(\dot{\omega}_d - \frac{|\Delta\omega|_{max}}{|\Delta\beta|_{max}} \frac{1-\varepsilon}{\varepsilon} \dot{\beta} \text{sat} \left(\frac{(\omega - \omega_d)\beta}{\Delta_1} \right) \right) - a(F_{y1} + F_{y2}) \\ + b(F_{y3} + F_{y4}) - \frac{l_f}{2}(F_{x2} - F_{x1}) - \frac{l_r}{2}(F_{x4} - F_{x3}) - k_2 \text{sat} \left(\frac{\omega - \omega_d}{\Delta_2} \right) \end{aligned} \quad (21)$$

3.4. Direct Yaw Moment Distribution

Compared to traditional vehicles, distributed electric vehicles can flexibly distribute the required driving force among all four wheels. The primary objective of longitudinal force distribution in the vehicle is to achieve optimization goals by optimally distributing torque from each motor. This is carried out while ensuring that the longitudinal speed matches the ideal speed and meets the additional yaw moment required for stability control. Constraints such as the peak power of the drive motor and ground-adhesion conditions must be considered when performing longitudinal force distribution.

In this case, the allocation of the lower-level transverse moment is aimed at achieving the minimum loading rate among the four tires as the optimization objective for moment allocation. This is to ensure that the vehicle can maintain a significant lateral stability margin throughout the control process. The loading rate of the tires, in this context, is defined as:

$$\zeta_i = \frac{F_{xi}^2 + F_{yi}^2}{(\mu F_{zi})^2} \quad (22)$$

F_{xi} , F_{yi} and F_{zi} are the longitudinal, lateral, and vertical forces on the corresponding tires, and μ is the pavement-adhesion coefficient.

Longitudinal speed tracking requirements:

$$\frac{1}{m}F_{x1} + \frac{1}{m}F_{x2} + \frac{1}{m}F_{x3} + \frac{1}{m}F_{x4} = \dot{v}_x - v_y\omega \quad (23)$$

Yaw moment requirement:

$$-\frac{l_f}{2}F_{x1} + \frac{l_f}{2}F_{x2} - \frac{l_r}{2}F_{x3} + \frac{l_r}{2}F_{x4} = M_z \quad (24)$$

Considering that the longitudinal and lateral forces of the wheel are constrained by the friction circle inequality during the driving process:

$$\begin{cases} \sqrt{F_{xi}^2 + F_{yi}^2} \leq \mu \cdot F_{zi} \\ \frac{T_i}{R_e} \leq \mu F_{zi} \end{cases} \quad (25)$$

The limit the peak torque of the wheel motor:

$$\begin{bmatrix} \frac{-T_{max}}{R_e} \\ \frac{-T_{max}}{R_e} \\ \frac{-T_{max}}{R_e} \\ \frac{-T_{max}}{R_e} \end{bmatrix} \leq \begin{bmatrix} F_{x1} \\ F_{x2} \\ F_{x3} \\ F_{x4} \end{bmatrix} \leq \begin{bmatrix} \frac{T_{max}}{R_e} \\ \frac{T_{max}}{R_e} \\ \frac{T_{max}}{R_e} \\ \frac{T_{max}}{R_e} \end{bmatrix} \quad (26)$$

The maximum motor output torque is limited by the maximum electromagnetic torque of the motor, T_{max} is the maximum output torque of the motor, and R_e is the effective radius of the wheel at work.

4. Coordinated-Control Strategy

This article presents a control framework, as shown in Figure 5. After designing the AFS and DYC controllers separately, guidelines should be developed to coordinate controls appropriately.

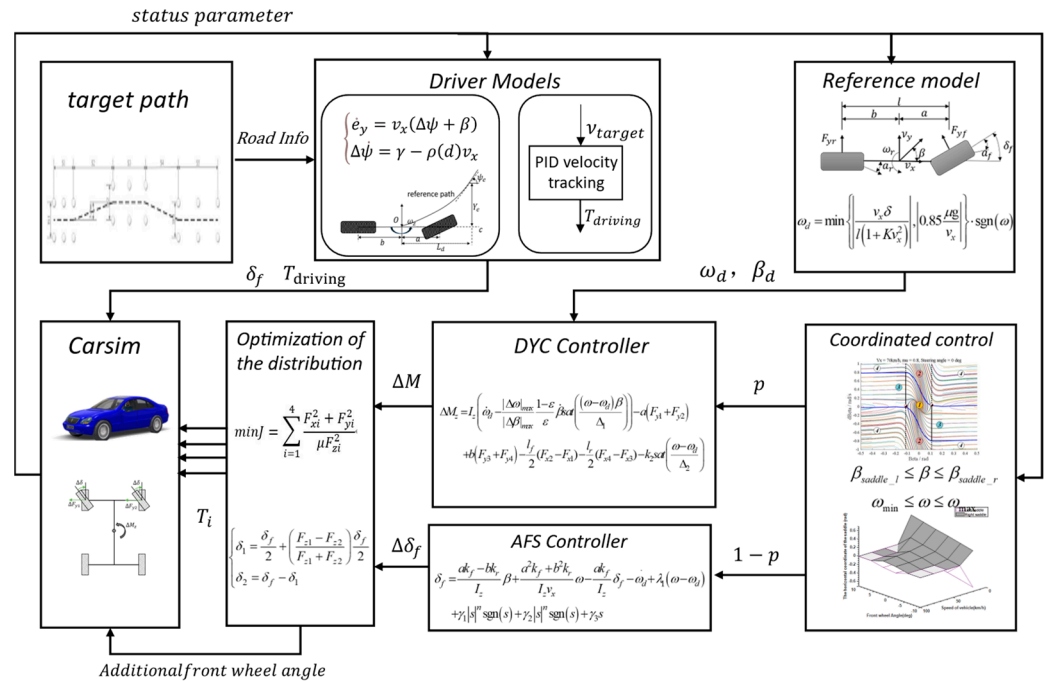


Figure 5. Coordination-control system structure.

The driver model outputs the front-wheel angle and performs longitudinal speed tracking based on pre-determined road information. The reference model outputs ideal state parameters based on the current vehicle speed and other information to provide input to the stability controller, while the coordination controller dynamically adjusts the stability controller weights in real time based on the current vehicle state and applies the optimized corner and wheel torque to the actuators.

Phase-plane stability analysis is often used for stability control of vehicle dynamics. In this paper, we use the 2-DOF vehicle equations to continuously traverse the phase-plane trajectory of $\beta - \dot{\beta}$ under different attachment coefficients, vehicle speeds, and front-wheel angles. The phase trajectory is represented by a color curve in the diagram, reflecting the change in vehicle state over time. After, we obtain phase-plane images, like those in Figure 6.

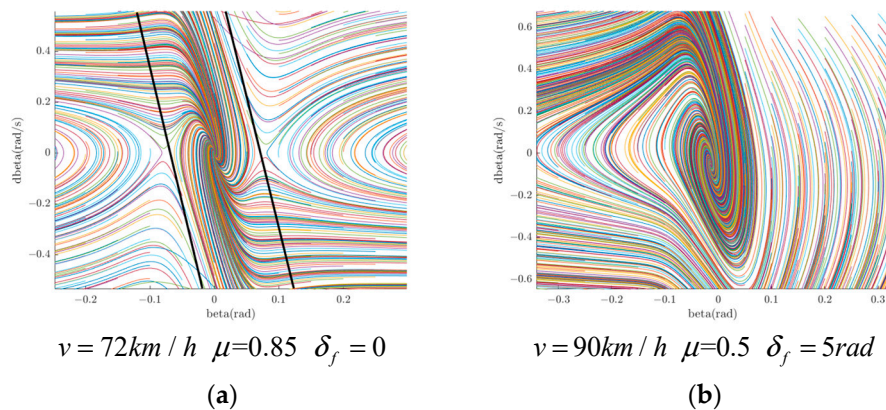


Figure 6. Phase plane (a) Stable boundary exists, (b) No stable boundary exists.

Figure 6 shows two cases: (a) where a stability boundary exists in the phase plane, and (b) where it does not. In case (b), the vehicle will eventually become unstable with any change in phase trajectory, regardless of its current state. Traditional studies often use the bilinear method to define the stability region. The method defines a stabilization region that is narrow and enveloped by two parallel straight lines [26], like in Figure 6a. The equation for the stability boundary can be expressed as:

$$\left| B_1\beta + B_2\dot{\beta} \right| < 1 \quad (27)$$

Some scholars have improved the traditional bilinear method, such as [27], but there is a drawback to this method. As long as the $\dot{\beta}$ is small enough, the vehicle is stable, even if the sideslip angle is large, as in Figure 7. The positions of the triangle in the figure are singularities.

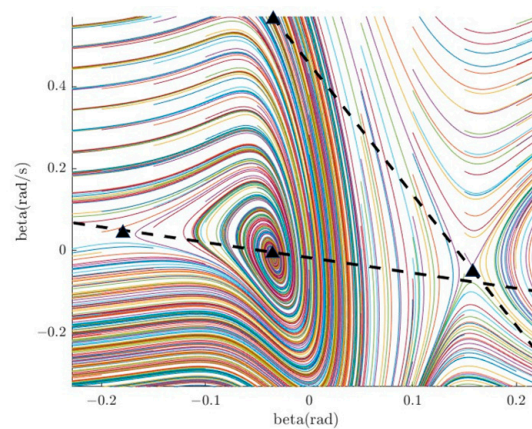


Figure 7. Stability region in $\beta - \dot{\beta}$ phase plane defined via double-line method.

However, it is known that excessive β can lead to vehicle instability. To make the delineation of the stability zones more rational, and at the same time extend the vehicle's stability control range as far as possible, we limit the angular velocity of the transverse pendulum. At the same time, the range of the sideslip angle is limited between the two saddle points to ensure better stability performance of the vehicle, and the divided phase plane is shown below to induce better stability performance of the vehicle. In view of the above two constraints, the phase-plane region is split again. The split phase plane is shown below.

As shown in Figure 8, the stability region is situated between the two saddle points of the phase plane, while also satisfying the stability criteria for vehicle yaw rate. Hence, the stabilization region can be expressed in the following constrained form:

$$\begin{cases} \beta_1 \leq \beta \leq \beta_2 \\ -\left| 0.85 \frac{\mu g}{v_x} \right| \leq \omega \leq \left| 0.85 \frac{\mu g}{v_x} \right| \end{cases} \quad (28)$$

The main challenge in the given equation is to identify the position of the saddle point. The saddle-point position depends mainly on the road surface-adhesion coefficient, vehicle speed, and front-wheel angle, and the phase-plane saddle-point position is obtained by iterating the above parameters in the feasible domain. The obtained saddle-point position image is shown in Figure 9.

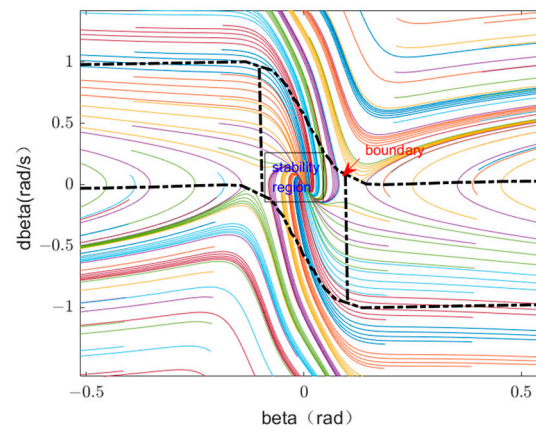


Figure 8. Phase-plane stability region partitioning.

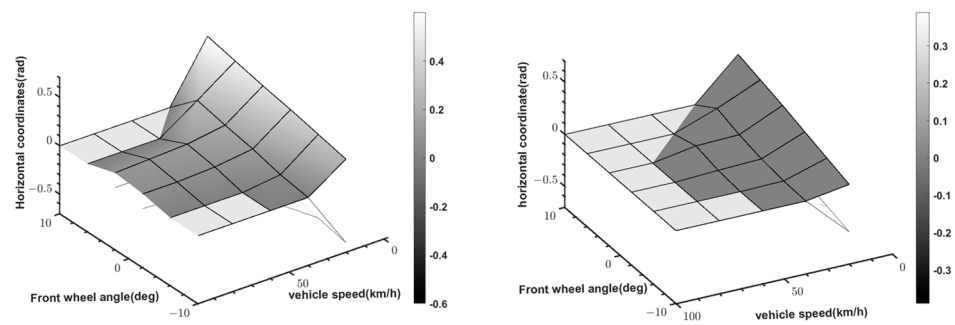


Figure 9. Horizontal coordinates of left and right saddle points.

To determine the extent of deviation of the current vehicle state from the ideal stability region defined in the previous section, we define the integrated deviation as I_{dis} . This includes the distance of the current sideslip angle position from the saddle point and the distance of the current yaw rate from the boundary conditions. We adopt the dimensionless method to weigh the two kinds of deviation and ultimately obtain the expression of the integrated deviation as:

$$I_{dis} = \frac{1 - \varepsilon}{|\Delta\beta|_{\max}} \left[1 - 2 \cdot \text{sign}[(\beta_2 - \beta)(\beta - \beta_1)] * \frac{\min(|\beta_2 - \beta|, |\beta - \beta_1|)}{\beta_2 - \beta_1} \right] + \frac{\varepsilon}{|\Delta\omega|_{\max}} \left[1 - 2 \cdot \text{sign}[(\omega_{\max} - \omega)(\omega - \omega_{\min})] * \frac{\min(|\omega_{\max} - \omega|, |\omega - \omega_{\min}|)}{\omega_{\max} - \omega_{\min}} \right] \quad (29)$$

When the degree of vehicle destabilization is low, only AFS alone is required for stability control, while as the vehicle gradually moves away from the stabilized state, DYC intervention is required with gradually increasing weights. It should be noted that the vehicle faces the switching of the control system in the critical state, which will have an impact on the maneuverability of the vehicle. In order to guarantee the smoothness of the whole control process, the switching function is designed with the help of the form of the boundary probability density function of the normal distribution, which dynamically adjusts the weight of the AFS and the DYC control in the coordinated-control process. Considering it is too late to engage the stability control strategy after destabilization, it is necessary to add a critical stability region, which is used to smoothly transition from the AFS control strategy to the DYC control strategy to ensure that the vehicle can be effectively controlled before destabilization. Based on this, the region within 0.625~1 of the steady state is taken as the critical stability region for the stability control algorithms:

$$p = \begin{cases} 0, & I_{dis} < 0.625 \\ \frac{1}{e^{\frac{(I_{dis}-\mu)^2}{2\delta^2}}}, & 0.625 < I_{dis} < 1 \\ 1, & I_{dis} > 1 \end{cases} \quad (30)$$

The parameter μ is defined in the above equation as 0.825, and δ is 0.125. From this, the intervention weights of AFS and DYC in coordinated control can be determined according to the current speed and attachment coefficients, etc. At the same time, it should be ensured that the two sub-systems are relatively smooth in their interventions and exits, to avoid a large impact in the process of system switching. The graph of the switching function is shown in Figure 10.

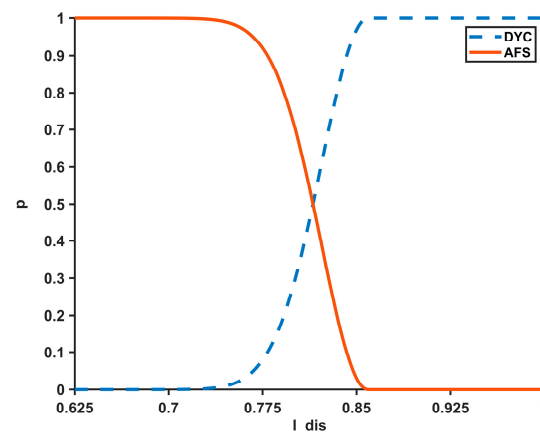


Figure 10. The weight of system intervention changes with I_{dis} .

5. Simulation Results

In order to verify the effectiveness of the coordinated-control strategy designed in this paper, based on the Carsim/Simulink joint simulation platform, a simulation was carried out for the double-lane change and snake-lane change conditions under different road-adhesion coefficients and vehicle speeds. In order to better evaluate the control effect of the coordinated controller designed in this paper, the designs of uncontrolled and ordinary integrated control are used as comparisons, in which the uncontrol group provides only the longitudinal speed tracking of the required wheel torque without interfering with the vehicle torque using stability control methods, while the integrated control uses fixed weights to distribute the lateral moment to the controllers. This involves a list of vehicle parameters, as shown in Table 1.

Table 1. Main parameters of the simulated vehicle.

Name	Symbolic	Value
Total vehicle mass	m	1415 kg
Front axis to center of mass	a	1.015 m
Rear axis to center of mass	b	1.895 m
Moment of inertia	I_z	1536.7 kg/m ²
Equivalent lateral deflection stiffness	k_f	−107,610 N/rad ^{−1}
Rear axle lateral deflection stiffness	k_r	−74.520/rad ^{−1}
Height of center of mass above ground	h_g	0.54 m
Rolling radius	R_e	0.325 m
Gravity acceleration	g	9.8 m/s ²
Peak torque of motor	T_{max}	350 [N*M]
Motor equivalent damping ratio	ζ	0.05

Double-lane change:

A closed-loop simulation experiment of double-lane change was carried out at a constant speed of 90 km/h and a road surface with a coefficient of adhesion of 0.85. The simulation results are shown in Figure 11. It can be observed that both integrated control and coordinated control can achieve a good tracking of the desired yaw rate at a speed of 90km/h and a high road-adhesion coefficient, and the results show that the vehicle stability under the coordinated-control strategy outperforms that under the integrated control. In terms of the sideslip angle, the actual value under coordinated control is closer to the desired zero value—the maximum value is 26.47% lower than that of integrated control, and the minimum value is 17.32% lower. In terms of lateral acceleration, coordinated control performs relatively better than integrated control in suppressing lateral acceleration, whereas the maximum value of the coordinated control is reduced by 18.76% and the minimum value is reduced by 12.78% compared with that of integrated control. Less lateral acceleration means better roll resistance. The double-lane change test shows that the coordinated control of AFS and DYC utilizes the ground-adhesion force better and can improve maneuvering stability while the vehicle performs lane-changing or lane-shifting operations.

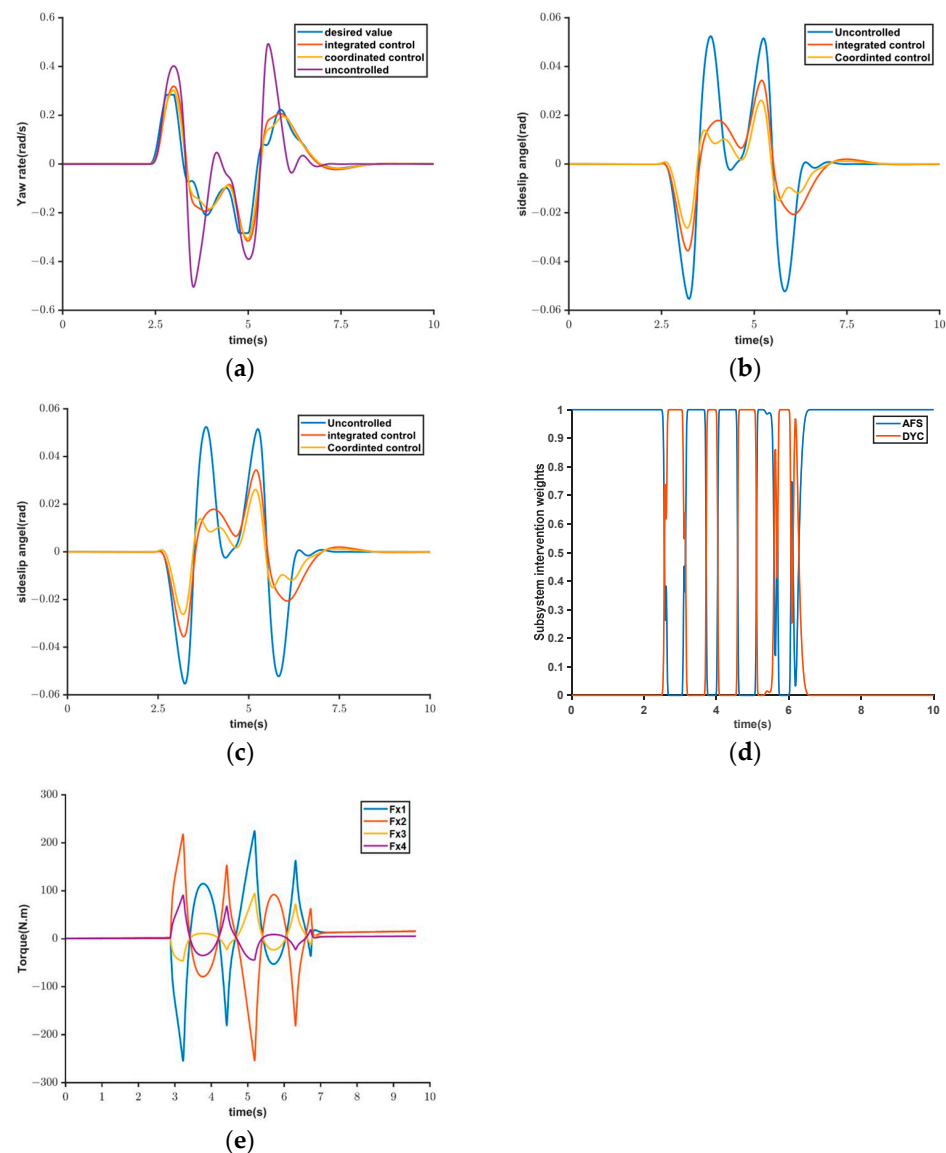


Figure 11. Simulation results under double-lane change: (a) yaw rate; (b) sideslip angle; (c) lateral accelerations; (d) weight of AFS and DYC; (e) wheel torque distribution.

Snake-lane change:

To comprehensively assess the merits and drawbacks of the control strategy, a serpentine condition experiment was conducted on the road surface at a speed of 100 km/h, with an adhesion coefficient of 0.8. The simulation duration was set at 15 s. Snake-lane changing at high speeds is a more effective test of the controller's performance under extreme conditions than a double-lane change.

Regarding the yaw rate in Figure 12a, it was observed that the uncontrolled vehicle experiences a sudden change after 2.5 s and is unable to accurately track the ideal value. On the other hand, the vehicle with integrated and coordinated control can successfully complete the tracking of the transverse angular velocity. The curve of the coordinated control is also much closer to the ideal curve. Figure 12b better corroborates the points made in this paper. The lateral deflections of the uncontrolled vehicle's sideslip angle showed instability after successive lane changes, whereas the coordinated-control sideslip angle remained within a small range and was better than a normal integrated controller in terms of stability.

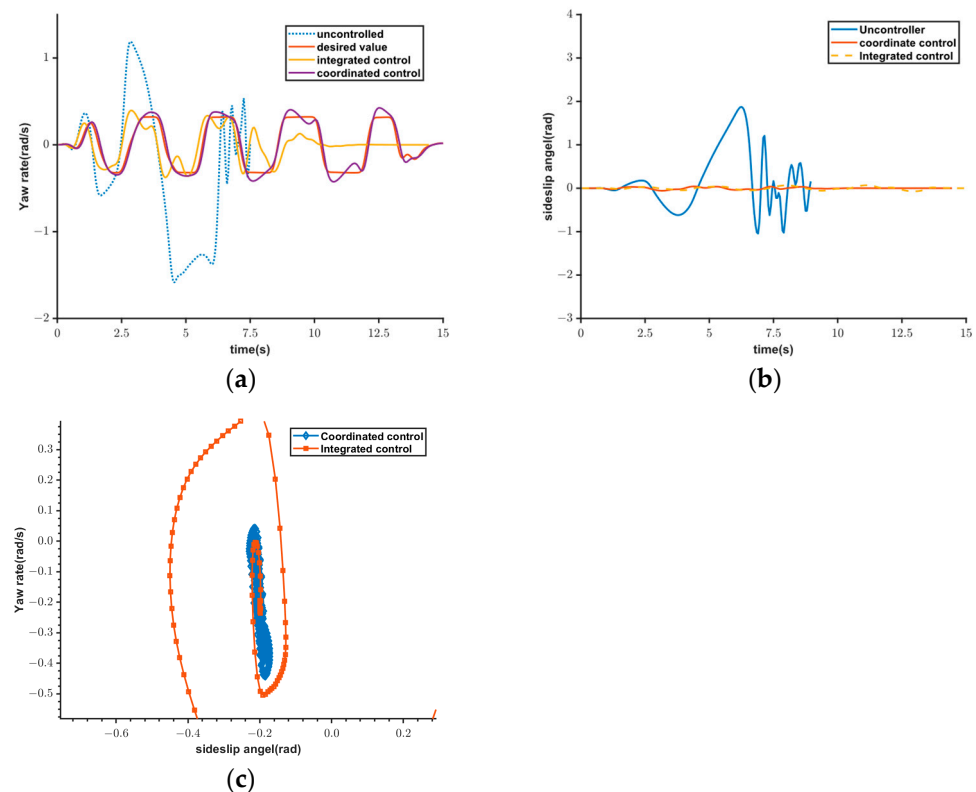


Figure 12. Simulation results under snake lane change: (a) yaw rate; (b) sideslip angle; (c) $\beta\omega$ phase plane.

It can be derived from Figure 12c that both control trajectories' phase planes reconverged to the origin. However, the phase trajectories of the maneuvering stability control phase-plane plot were notably closer to the center of stability and exhibited an even distribution. This suggests that the maneuvering stability control enhances stability during snake-lane change conditions.

The research findings indicate that the control strategy proposed in this paper results in a minimal lateral deflection angle of the center of mass, yaw rate, and lateral acceleration. Moreover, it achieves a higher level of tracking accuracy.

6. Conclusions

In this paper, a novel vehicle-stability coordinated-control algorithm is proposed. In terms of controller design, a hierarchical control approach is adopted to optimally distribute the outputs of the upper-level controller to actuators, ensuring the vehicle has a satisfactory stability margin. Regarding coordinated control, the authors optimize the traditional bilinear method by redefining the stability region of the phase plane based on saddle-point positions and lateral angular velocity thresholds. Furthermore, the intervention weights of the two sub-controllers are dynamically adjusted based on the extent of deviation of the current vehicle state from the stable state.

The results of the simulation demonstrate that the coordinated-control algorithms proposed in this paper are more effective in fulfilling the performance requirements of vehicle stability and enhancing the stability margin of the vehicle to handle extreme working conditions when operating at varying speeds and road-adhesion coefficients.

However, there are many issues that are not discussed in depth in this paper. For example, the working condition set in this paper involves a constant longitudinal velocity, and the tire-road friction coefficient is kept constant in the same simulated working condition. This will be considered in future research to make the ideas in this article more relevant.

Author Contributions: Conceptualization, J.L. and A.D.; methodology, A.D.; software, A.D.; validation, J.L., A.D.; formal analysis, A.D.; investigation, A.D.; resources, J.L.; data curation, J.L.; writing—original draft preparation, A.D.; writing—review and editing, A.D.; visualization, A.D.; supervision, J.L. All authors have read and agreed to the published version of the manuscript.

Funding: This research received no external funding.

Data Availability Statement: The original contributions presented in the study are included in the article. Further inquiries can be directed to the corresponding author.

Conflicts of Interest: The authors declare no conflicts of interest.

References

1. Jing, C.; Shu, H.; Song, Y.; Wu, T. Active front steering control strategy based on estimation of vehicle state and mass identification. *Int. J. Veh. Noise Vib.* **2021**, *17*, 253–272. [[CrossRef](#)]
2. Zhang, J.; Wang, H.; Ma, M.; Yu, M.; Chen, L. Active front steering-based electronic stability control for steer-by-wire vehicles via terminal sliding mode and extreme learning machine. *IEEE Trans. Veh. Technol.* **2020**, *69*, 14713–14726. [[CrossRef](#)]
3. Ma, L.; Mei, K.; Ding, S. Direct yaw-moment control design for in-wheel electric vehicle with composite terminal sliding mode. *Nonlinear Dyn.* **2023**, *111*, 17141–17156. [[CrossRef](#)]
4. Ding, S.; Liu, L.; Zheng, W.X. Sliding mode direct yaw-moment control design for in-wheel electric vehicles. *IEEE Trans. Ind. Electron.* **2017**, *64*, 6752–6762. [[CrossRef](#)]
5. Xuanhao, C.; Kai, H.; Yufeng, L.; Yantao, T. Direct Yaw Moment Control of Electric Vehicle for Improving the Vehicle Lateral Stability. In Proceedings of the 2018 IEEE International Conference on Mechatronics and Automation (ICMA), Changchun, China, 5–8 August 2018.
6. Nagai, M.; Shino, M.; Gao, F. Study on integrated control of active front steer angle and direct yaw moment. *Jsaev Rev.* **2002**, *23*, 309–315. [[CrossRef](#)]
7. Mashadi, B.; Majidi, M. Integrated AFS and DYC Sliding Mode Controller Design for Hybrid Electric Vehicle. In Proceedings of the ASME 2010 10th Biennial Conference on Engineering Systems Design and Analysis, Istanbul, Turkey, 12–14 July 2010.
8. Wang, L.; Liu, G.; Zhang, D.; Miao, P. Integrated control of active front steering and direct yaw moment for multi-wheel independently driven electric vehicles. In Proceedings of the 2013 International Conference on Electrical Machines and Systems (ICEMS), Busan, Republic of Korea, 26–29 October 2013.
9. Chen, W.; Liang, X.; Wang, Q.; Zhao, L.; Wang, X. Extension coordinated control of four wheel independent drive electric vehicles by AFS and DYC. *Control Eng. Pract.* **2020**, *101*, 104504. [[CrossRef](#)]
10. Wu, X.; Zhou, B.; Wu, T.; Pan, Q. Research on intervention criterion and stability coordinated control of afs and dyc. *Int. J. Veh. Des.* **2022**, *90*, 116–141. [[CrossRef](#)]
11. Liu, J.; Liu, H.; Wang, J.; Gu, H. Coordinated Lateral Stability Control of Autonomous Vehicles Based on State Estimation and Path Tracking. *Machines* **2023**, *11*, 328. [[CrossRef](#)]
12. Zhang, L.; Ma, L.; Chen, S. Design of the integrated afs and dyc scheme for vehicles via fsm and sosm techniques. *Discret. Contin. Dyn. Syst. S* **2022**, *15*, 3331–3350. [[CrossRef](#)]
13. Zhai, L.; Sun, T.; Wang, J. Electronic stability control based on motor driving and braking torque distribution for a four in-wheel motor drive electric vehicle. *IEEE Trans. Veh. Technol.* **2016**, *65*, 4726–4739. [[CrossRef](#)]

14. Jin, X.; Yu, Z.; Yin, G.; Wang, J. Improving vehicle handling stability based on combined afs and dyc system via robust takagi-sugeno fuzzy control. *IEEE Trans. Intell. Transp. Syst.* **2017**, *19*, 2696–2707. [[CrossRef](#)]
15. Li, H.; Wu, C.; Jing, X.; Wu, L. Fuzzy tracking control for nonlinear networked systems. *IEEE Trans. Cybern.* **2016**, *47*, 2020–2031. [[CrossRef](#)]
16. Zhang, L.; Zhang, Z.; Wang, Z.; Deng, J.; Dorrell, D.G. Chassis coordinated control for full x-by-wire vehicles-a review. *Chin. J. Mech. Eng.* **2021**, *34*, 42. [[CrossRef](#)]
17. Jing, C.Q.; Shu, H.Y.; Shu, R.; Song, Y. Integrated control of electric vehicles based on active front steering and model predictive control. *Control. Eng. Pract.* **2022**, *121*, 105066. [[CrossRef](#)]
18. Pacejka, H.B. *Tire and Vehicle Dynamics*, 3rd ed.; Elsevier: Amsterdam, The Netherlands, 2012; pp. xiii–xvi.
19. Goryca, J.E. *Force and Moment Plots from Pacejka 2002 Magic Formula Tire Model Coefficients*; US Army Research, Development and Engineering Command: Warren, MI, USA, 2010.
20. Bakker, E.; Nyborg, L.; Pacejka, H.B. Tyre modeling for use in vehicle dynamics studies. *SAE Trans.* **1987**, *96*, 190–204.
21. Huang, Q.; Huang, Q.; Guo, H.; Cao, J. Design and research of permanent magnet synchronous motor controller for electric vehicle. *Energy Sci. Eng.* **2023**, *11*, 112–126. [[CrossRef](#)]
22. Tahami, F.; Kazemi, R.; Farhanghi, S. A novel driver assist stability system for all-wheel-drive electric vehicles. *IEEE Trans. Veh. Technol.* **2003**, *52*, 683–692. [[CrossRef](#)]
23. Zhou, H.; Liu, Z. Vehicle yaw stability-control system design based on sliding mode and backstepping control approach. *IEEE Trans. Veh. Technol.* **2010**, *59*, 3674–3678. [[CrossRef](#)]
24. Zhang, J.; Zhou, S.; Li, F.; Zhao, J. Integrated nonlinear robust adaptive control for active front steering and direct yaw moment control systems with uncertainty observer. *Trans. Inst. Meas. Control* **2020**, *42*, 3267–3280. [[CrossRef](#)]
25. Fu, C.; Hoseinnezhad, R.; Li, K.; Hu, M. A novel adaptive sliding mode control approach for electric vehicle direct yaw-moment control. *Adv. Mech. Eng.* **2018**, *10*, 1687814018803179. [[CrossRef](#)]
26. Zhang, X.; Göhlich, D. Integrated traction control strategy for distributed drive electric vehicles with improvement of economy and longitudinal driving stability. *Energies* **2017**, *10*, 126. [[CrossRef](#)]
27. Ko, Y.E.; Lee, J.M. Estimation of the stability region of a vehicle in plane motion using a topological approach. *Int. J. Veh. Des.* **2002**, *30*, 181–192. [[CrossRef](#)]

Disclaimer/Publisher’s Note: The statements, opinions and data contained in all publications are solely those of the individual author(s) and contributor(s) and not of MDPI and/or the editor(s). MDPI and/or the editor(s) disclaim responsibility for any injury to people or property resulting from any ideas, methods, instructions or products referred to in the content.